Shin et al. *NPG Asia Materials* (2023) 15:54
https://doi.org/10.1038/s41427-023-00502-y

NPG Asia Materials

ARTICLE Open Access

Rational engineering of high-entropy oxides for Li-ion battery anodes with finely tuned combustion syntheses

Dongjoon Shin[1], Seunghoon Chae[1], Seonghyun Park[1], Byungseok Seo[1] and Wonjoon Choi[1]

Abstract

High-entropy oxides (HEOs) are promising conversion-type anode materials for Li-ion batteries (LIBs) owing to their excellent cycling stabilities and rate capabilities. However, the conventional syntheses and screening processes are time-consuming and complex and require phase and interfacial segregation of individual elements. Herein, we report a rational screening strategy for LIB anodes using precisely tunable HEOs fabricated by one-step combustion syntheses with different fuel-to-oxidizer ratios (φ). A slightly lean fuel mixture (φ-0.95) enabled a suitable temperature and non-reducing atmosphere for optimal HEO syntheses. This provided high crystallinity, perfectly homogeneous elemental distributions, and adequate pore structures without selective precipitation, whereas lower or higher fuel-to-oxidizer ratios resulted in excessively porous morphologies or elemental segregation. HEO-based anodes with φ-0.95 exhibited outstanding specific capacities (1165 mAh g^{-1}, 80.9% retention at 0.1 A g^{-1}, and 791 mAh g^{-1} even at 3 A g^{-1}), excellent rate capabilities, and stable cycling lifetimes (1252 mAh g^{-1}, 80.9% retention after 100 cycles at 0.2 A g^{-1}). This design strategy will provide fascinating HEO electrodes that cannot be prepared with conventional fabrication methods.

Introduction

Lithium-ion batteries (LIBs) have become increasingly important for various small- to large-scale energy storage systems, such as mobile phones, portable electronics, and mobility platforms, including drones and electrical vehicles[1]. LIBs enable long-term operation under dynamic load conditions while packaged within restricted spaces. Thus, the development of advanced electrodes to increase LIB capacities has attracted considerable effort to reduce the volumes and weights of energy storage cells[2]. In particular, the low theoretical capacities (~372 mAh g^{-1}) of graphitic carbons, which are typically used as anode materials, should be resolved to overcome the fundamental limits of LIB performance[3,4].

As conversion-type anode materials, transition metal oxides (TMOs), such as CuO, Fe_2O_3, Co_3O_4, Fe_3O_4, and $NiFe_2O_4$, are promising candidates for achieving breakthroughs owing to their high specific capacities (700–1200 mAh g^{-1})[5,6]. However, the use of TMOs as anode materials leads to severe capacity-fading problems[7]. This critical feature results from mechanical degradation of the electrodes associated with pulverization of the active material and its detachment from binders due to the volume changes occurring during lithiation/delithiation cycling and the accumulation of an internal passivation layer that serves as a kinetic barrier[8]. Furthermore, because TMO-based anodes have intrinsically higher operating voltages than graphitic carbon and a slanted voltage curve, the capacities of TMOs must be high enough to mitigate these challenges after multiple charge/discharge cycles. Thus, achieving outstanding cyclic stability and rate capability in the electrochemical performance of TMO-based anodes remains challenging.

Correspondence: Wonjoon Choi (wojchoi@korea.ac.kr)
[1]School of Mechanical Engineering, Korea University, Seoul 02841, Republic of Korea
These authors contributed equally: Dongjoon Shin, Seunghoon Chae

Transition metal-based high-entropy oxides (HEOs) consisting of five or more cations have emerged as remarkable anode materials through exploitation of the advantages of their individual constituents, thereby improving the electrochemical capabilities of LIBs[9]. A HEO significantly improves the cycling stability and rate capability of the LIB via entropy stabilization, which is enabled by the high configurational entropy and synergistic effects of the metal ions. For instance, ex situ analyses of HEO characteristics have revealed that entropic stabilization for long-term cycling stability of HEO LIB anodes could originate from the nearby neighbors and metallic bonds for CoO, NiO, and CuO[10]. In addition, the crystalline structures of HEOs could be entirely disrupted during the conversion reaction of the first lithiation cycle, while the initial random distribution of metal atoms emerges as a primary factor influencing the capacity[11]. HEOs with rock-salt structures comprising electrochemically inactive cations (e.g., Mg) that prevent aggregation of the active materials, or Li, which increases the number of oxygen vacancies, have been introduced to obtain higher cycling stability and promote electronic and ionic conductivity of the electrodes[12,13]. Furthermore, HEOs with spinel structures could boost the reversible capacity, as two different Wyckoff sites of the spinel structure increased the range of valence states, unlike rock-salt structures with only one Wyckoff site[14–16]. In this respect, the potential of HEOs for use as LIB anode materials has been demonstrated in terms of their structural and compositional characteristics and electrochemical performance.

The conventional synthetic approaches to HEOs require complex procedures that incur high costs and require long processing times[17,18]. They commonly involve demanding operating conditions and pre- or posttreatments, which are time-consuming and energy-intensive[19]. In particular, conventional wet-chemistry syntheses limit the alloy composition to less than three elements, result in phase separation, and do not provide compositional and size uniformity[20]. Inhomogeneous mixing or impregnation during solution-based processing results in phase-separated or nonuniform structures of the immiscible elements of the HEO, which inhibits compositional flexibility. They tend to exist in multiple phases in which solid solutions are formed only between thermodynamically miscible elements. In addition, long-term exposure to high temperatures provides a favorable environment for nanoparticle agglomeration and species segregation, which further inhibits the formation of a homogeneous solid solution. The subsequent reduction procedures also result in phase separation between multimetallic oxides and do not provide structural complexity or flexibility. Although relatively facile fabrication methods for HEOs have recently been developed, including planetary ball milling, hydrothermal methods, and solution combustion syntheses, they have intrinsic limits in achieving precisely tailored HEOs because their products inevitably involve various impurities due to a failure to suppress the mixing enthalpy[16]. Moreover, additional processes, such as post-heating treatments for 12–24 h with a high-temperature furnace or bulky chamber, are required to compensate for the mixing enthalpy of the constituents. Therefore, more scalable yet precisely tunable fabrication routes for HEOs are essential for facilitating rapid syntheses/screening[21], thereby achieving rational development of HEO anode materials exhibiting optimal electrochemical performance.

Herein, we report the rational design of precisely tunable HEO composites with superior electrochemical characteristics, which were fabricated via facile one-step combustion processes using optimized fuel-to-oxidizer ratios and without any postprocessing, and their use in high-performance HEO LIB anodes (Fig. 1). The precursors of five transition metal elements (Mn, Fe, Co, Ni, and Cu) were merged into electrochemically active HEOs via combustion with glycine, which served as a fuel and chelating agent. Fuel-to-oxidizer ratios (φ) of 0.9, 0.95, 1.0, and 1.05 were used to control the major features of the synthesized HEOs, such as the phases, crystallinities, grain boundaries, configurational entropies, and morphological characteristics. By screening distinct phases, configuration entropies, and physicochemical characteristics, the HEOs were fabricated at suitable temperatures and in reducing environments (φ-0.95, a slightly lean fuel mixture) and exhibited ideal properties for use as the active materials of LIB anodes, such as high crystallinities, perfectly homogeneous elemental distributions, and adequately porous backbone structures. These optimal characteristics avoided size variations and inhibited structural failures. Moreover, the high proportion of the spinel phase without selective precipitation of the metallic compounds could have contributed to generation of the highest specific capacity. In contrast, lower or higher fuel to oxidizer ratios (φ-0.9, φ-1.0 and φ-1.05) led to the formation of excessively porous structures or segregation of the specific elements that degraded the electrochemical reactions. All HEO-based anodes exhibited excellent specific capacities, and the entropy stabilization effect contributed to their high cyclic stabilities. Among them, HEO-based anodes (with φ-0.95) exhibited outstanding specific capacities (1165 mAh g^{-1} at 0.1 A g^{-1} and 791 mAh g^{-1} even at 3 A g^{-1}) and excellent rates, as well as a stable cycling lifetimes (1252 mAh g^{-1} after 100 cycles at 0.2 A g^{-1}). Comparisons with other HEO-based anodes confirmed the high specific capacities and outstanding rates for the rationally mixed metal elements and combined structure during electrochemical processes. The design strategy offers extremely rapid yet

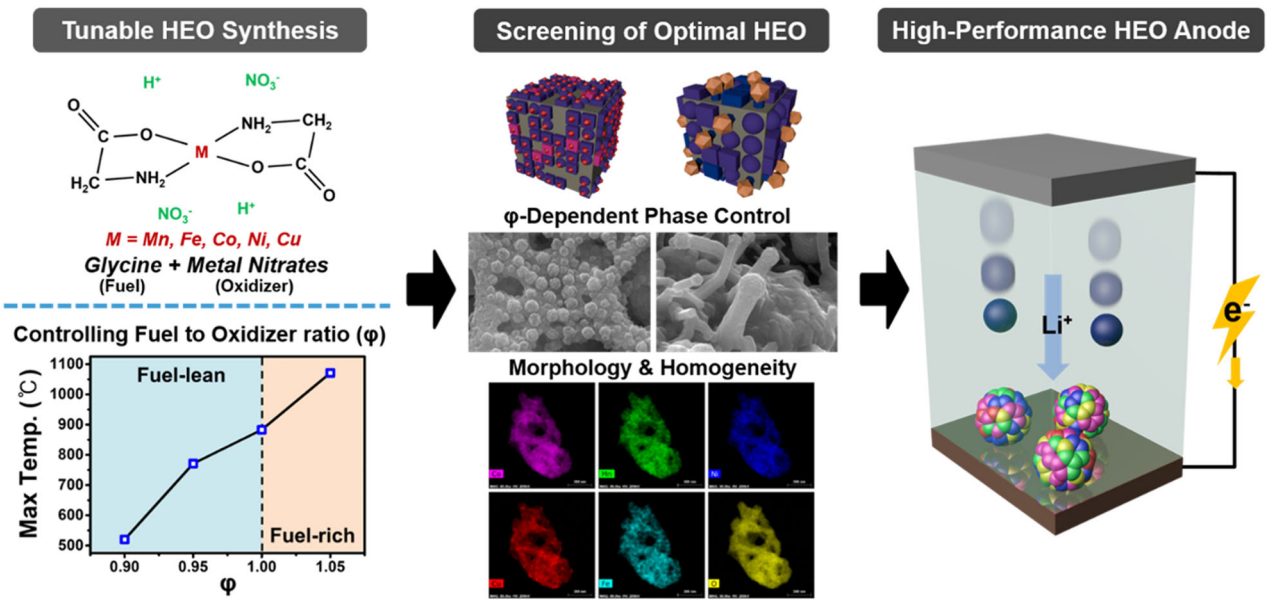

Fig. 1 Rational design of one-step combustion syntheses for precisely tunable HEO active materials for Li-ion battery anodes. The adjustable fuel-to-oxidizer ratios provided transitions of the crystalline structures and configurational entropies of the five transition metal elements (Mn, Fe, Co, Ni, Cu) to determine the optimal structures and phases of the HEO-based anodes.

precisely controlled fabrication routes for sorting and optimizing HEOs comprising multiple metal/metal oxides within homogeneously mixed compositions. This is potentially useful for a range of applications, such as with electrodes, catalysts, thermal barrier coatings, and thin-film transistors.

$$\varphi_e = \frac{\sum(Coefficient\ of\ reducing\ elements\ in\ specific\ formula) * (reducing\ valency) * (molar\ coefficient)}{(-1)\sum(Coefficient\ of\ reducing\ elements\ in\ specific\ formula) * (oxidizing\ valency) * (molar\ coefficient)} \quad (1)$$

Materials and methods

Chemicals and materials

Iron(III) nitrate nonahydrate ($Fe(NO_3)_3{\cdot}9H_2O$), manganese(II) nitrate tetrahydrate ($Mn(NO_3)_2{\cdot}4H_2O$), nickel(II) nitrate hexahydrate ($Ni(NO_3)_2{\cdot}6H_2O$), copper(II) nitrate trihydrate ($Cu(NO_3)_2{\cdot}H_2O$), and cobalt(II) nitrate hexahydrate ($Co(NO_3)_2{\cdot}6H_2O$) were prepared as precursors for the syntheses of the HEOs, while glycine served both as a fuel and a chelating agent. All chemicals were purchased from Sigma–Aldrich (USA) and were used as received without further purification.

Tunable fabrication of HEO composites via combustion syntheses

Nitrates with equimolar concentrations of 0.2 M (Fe, Mn, Ni, Cu, Co) and glycine with different fuel-to-oxidizer ratios (φ-0.9, φ-0.95, φ-1.0, and φ-1.05) were dissolved in 20 ml of DI water and homogeneously mixed under magnetic stirring for 1 h. The fuel-to-oxidizer ratios were calculated with the following equation, while the relative ratios of the reactants and products for each condition were estimated from the chemical reaction stoichiometries (Supplementary Information, Supplementary Note 1).

Afterward, the resulting mixture was placed on a hot plate and heated at 300 °C until the combustion process was completed. The products were the HEO powders that were used as the active materials for the anodes.

Characterization of the Materials

Two optical pyrometers (Raytek RAYMM2MLCF1L and Raytek RAYMM1MHCF1L with temperature ranges of 300 to 1100 °C and 540 to 3000 °C, respectively) were used to measure the real-time temperatures during the combustion syntheses. The first pyrometer with the lower temperature range was used to measure the temperature of φ-0.9, while the second pyrometer with the higher temperature range was used for φ-0.95, φ-1.0 and φ-1.05. The phases of the synthesized HEO products were characterized by X-ray diffraction (XRD, Rigaku Smartlab) using Cu Kα radiation ($\lambda = 0.14512$ nm) at 45 kV and 200 mA. The HEO powders were scanned over a 2θ range

of 20°–90° at a scan rate of 1°/min. The morphologies and structures of the as-prepared samples were investigated with electron microscopy and EDS elemental mapping with field-emission scanning electron microscopy (FE-SEM, FEI Quanta 250 FEG) and transmission electron microscopy (TEM, Tecnai F20 G2). The chemical components and valences of the samples were examined with X-ray photoelectron spectroscopy (XPS, Ulvac-phi X-tool).

Electrochemical measurements and characterization

An HEO anode was prepared by mixing the HEO active materials synthesized as described above, carbon black, and a CMC/SBR binder to form a slurry. The weight ratios of the slurries for all prepared anodes were 7:2:1 for the active materials, carbon black, and the CMC/SBR binder. After casting onto a copper foil using a doctor blade, the slurry was dried in a vacuum oven at 60 °C for more than 12 h to completely remove any moisture from the electrode. The loading density of the active material in the dried electrode was approximately 1 mg/cm^2. Thereafter, a circular disc with a diameter of 15 mm was punched out to form the dried electrode. The cut electrodes were assembled into CR2032 coin cells with lithium chips (~16 mm in diameter) and 25-μm thick Celgard PE separators in a glove box with an H_2O content < 0.1 ppm and an O_2 content < 0.1 ppm. In the coin cells, 1 M $LiPF_6$ EC:DEC:DMC (v:v 1:1:1) was used as the electrolyte. The assembled coin cells were tested with a WBCS3000 battery tester (WonATech). To determine the redox mechanisms of the HEO electrodes synthesized with different fuel-to-oxidizer ratios, 3 charging and discharging cycles were applied within a voltage window of 0.01 to 3.0 V at a scan rate of 0.1 mV/s. In comparing the rate capabilities, galvanostatic charge–discharge tests were conducted after every 5 cycles with current densities of 0.1, 0.2, 0.5, 1.0, 2.0, 3.0, and 0.1 A g^{-1} within the voltage window 0.01 to 3.0 V. The long term cycling stability was investigated with a current density of 0.2 A g^{-1} in the 0.01–3 V range. Electrochemical impedance spectroscopy (EIS) was performed in the frequency range of 10^6–0.1 Hz with an amplitude of 10 mV using a Zive MP1 system (WonA Tech).

Results and discussion

Tunable combustion syntheses for screening the HEOs

The elements Mn, Fe, Co, Ni, and Cu were selected as HEO substrates because of their similar atomic radii and good solubilities, and the resulting HEOs exhibited stable structures and excellent stabilities during charge–discharge cycling due to entropy stabilization. The HEO composites comprising Mn, Fe, Co, Ni, and Cu were fabricated through combustion syntheses by employing different stoichiometric ratios, thereby precisely adjusting the physicochemical characteristics (Fig. 1). Screening of the transition metal elements considered the electrochemical and thermodynamic properties, such as capacity and entropy stabilization. Homogeneous precursor solutions were prepared by mixing the selected metal nitrates and glycine with different fuel-to-oxidizer ratios (φ-0.9, φ-0.95, φ-1.0, and φ-1.05) and magnetically stirring the constituents in DI water. Afterward, facile yet effective solution combustion syntheses led to the HEO powders in one step and without any posttreatment. As the precursor solution became viscous and black during stirring and heating at 300 °C, self-propagating combustion occurred instantly, resulting in the formation of black fluffy HEO powder. During this exothermic chemical reaction, glycine served as both a fuel and a chelating agent owing to its carboxylic acid and amino groups. Thus, it prevented selective precipitation and provided a homogeneous distribution of the five elements in the precursor solution.

Physical and chemical characterization of the HEO composites

The HEO composites were produced with precise control of the different fuel-to-oxidizer ratios, and their crystalline structures were elucidated with X-ray diffraction (XRD, Fig. 2a). First, the fuel-lean ratios of 0.9 and 0.95 resulted in a background peak at 22°, indicating amorphous carbon produced by incomplete combustion. As the φ values exceeded 1, the carbon peak disappeared because of the stoichiometric composition reaction. Additionally, the remaining HEO composites exhibited peaks for the spinel (JCPDS # 00-001-1110, $NiMn_2O_4$) and rock-salt (JCPDS #47-1049, NiO) phases. More specifically, when combustion syntheses were implemented with φ values below 0.9, the peaks for the spinel phase were dominant, and the rock-salt phase was a secondary phase. A low combustion temperature for the φ-0.9 mixture inhibited the growth of crystalline grains, thereby resulting in a broad XRD peak indicating a poorly crystalline material. As the fuel-to-oxidizer ratios were increased, elevated temperatures were used for the HEO syntheses, and relatively sharper XRD peaks were obtained. For instance, the additional diffraction peaks seen at 43.63° and 50.83° for the φ-1.05 mixture corresponded to $Cu_{0.81}Ni_{0.19}$ (JCPDS # 00-047-1406). Increasing the fuel-to-oxidizer ratio enabled the use of a more reducing ambient environment (CO and H_2) and resulted in a decrease in the partial pressure of O_2 needed for combustion. These analyses indicated that some of the copper oxide and nickel oxide were reduced, thereby resulting in the presence of a copper-nickel alloy[22]. Further analyses of the XRD patterns were performed after Rietveld refinement (Supplementary Fig. S2) of the dataset and were focused on the phase volume fractions, cell parameters, and grain sizes (Supplementary Table S1). As

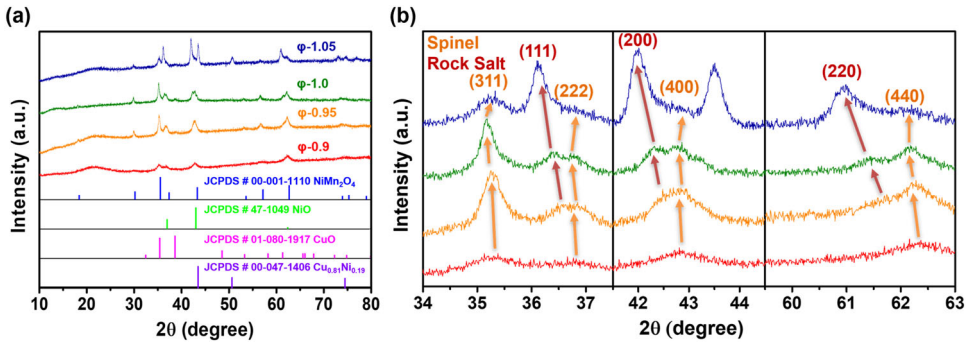

Fig. 2 XRD patterns of the HEO composites fabricated by combustion syntheses. XRD profiles of (**a**) HEO powders synthesized with different fuel-to-oxidizer ratios (φ-0.9, φ-0.95, φ-1, and φ-1.05) and (**b**) peak shifts for the spinel and rock-salt phases according to the φ value.

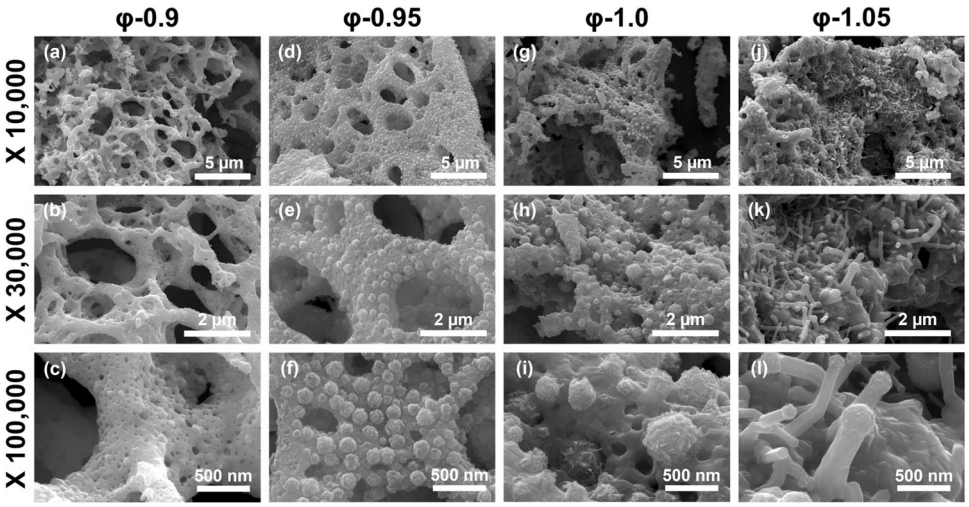

Fig. 3 Morphological transitions of the HEO composites enabled by tunable combustion syntheses. Scanning electron microscopy (SEM) images of the HEO composites fabricated with different fuel-to-oxidizer ratios of (**a**–**c**) φ-0.9, (**d**–**f**) φ-0.95, (**g**–**i**) φ-1.0, and (**j**–**l**) φ-1.05. The magnification varied between 10,000 and ×100,000.

the fuel-to-oxidizer ratio was increased, the proportion of the spinel phase decreased. Consumption of the oxygen species induced by the reducing atmosphere caused an instant reduction in the spinel to rock-salt, monoclinic, and metal phases[23]. Additionally, the diffraction peaks for the (311), (222), (400), and (440) planes of the main spinel lattices and the (111), (200), and (220) planes of the main cubic rock-salt metal-oxide peaks shifted to the left with increased φ value of 0.95 and 1.0, respectively, indicating increases in the d spacings (Fig. 2b). Moreover, the rock-salt peaks shifted to the left for the φ-1.05 mixture, in contrast to the spinel peaks. The changes in the cell parameters confirmed that particular cations, such as Cu^{2+} and Ni^{2+}, in the spinel or rock-salt structures were replaced by other ions with larger sizes and that they were separated into monoclinic CuO or Cu-Ni metal phases under the stronger reducing atmospheres (φ-1.0 and φ-1.05). Therefore, the secondary rock-salt phase appeared for φ-1.0 and φ-1.05 because the separation and reduction of copper and nickel led to the formation of additional phases via thermal reoxidation. The larger grain sizes obtained with the higher temperatures used for combustion with higher fuel-to-oxidizer ratios were identified with the aid of the Rietveld refinements.

The morphological transitions seen for different fuel-to-oxidizer ratios were investigated with scanning electron microscopy (SEM) (Fig. 3). The nano/microstructures synthesized in the one-step combustion process showed that the constituent nanoparticles were uniformly spread and agglomerated, thereby completing the porous framework. During the exothermic reaction occurring during the combustion process, the large amounts of gas liberated during nucleation of the oxides prevented the growth of crystals and produced the porous structures. In detail, the low fuel-to-oxidizer ratio (φ-0.9) resulted in the smallest particle dimensions without significant

aggregation, while large pores appeared in the structures (Fig. 3a–c). In the combustion process with a fuel-to-oxidizer ratio of φ-0.95, agglomerated nanoparticles (<100 nm) appeared on the porous backbone with smaller pore sizes in comparison with those of the φ-0.9 mixture (Fig. 3d–f). Furthermore, as the stoichiometric ratio was increased to φ-1.0, the porosity obviously decreased, and the nanoparticles were enlarged by agglomeration (Fig. 3g–i). The average diameters of the spherical nanoparticles fabricated with φ-0.9, φ-0.95, and φ-1.0 were approximately 61 nm, 110 nm, and 203 nm, respectively, and all of the particles were anchored to the porous backbones without interfacial boundaries. Additionally, the nanostructures fabricated in the combustion synthesis with φ-1.05 revealed a distinct transition, which was classified with other fuel-to-oxidizer ratios (Fig. 3j–l). The spherical particles gradually protruded from the exposed surfaces of the porous backbones, and the growth of nanorods with spherical particles on the tops was observed.

Energy dispersive spectrometry (EDS) and areal mapping of the synthesized materials indicated the homogeneities of the transition metal cations and the cation-to-oxygen ratio (Figs. S3, S4). The slightly higher manganese atomic ratio was attributed to variations in the sample topography, resulting in different signal intensities for the elements during EDS signal acquisition. The cation compositions and distributions were nearly identical in all cases, thereby implying the presence of homogeneously mixed HEOs, whereas the relative proportion of oxygen decreased as the fuel-to-oxidizer ratio (φ) was increased. Because the excess fuel consumed more oxygen during the combustion process, it led to the separation of the copper and reduction of the copper oxides. Point EDS maps of the spherical nanoparticles and nanorods synthesized during the combustion syntheses with φ-0.95, φ-1.0, and φ-1.05 were used to analyze the specific elemental distributions (Supplementary Fig. S5). The atomic ratio of copper was higher in all spherical particles than those of the other constituent metals, and the ratios increased with higher φ values (Supplementary Fig. S5a–c). These EDS maps indicated that copper was partially reduced from a higher oxidation state (spinel and rock salt) to a lower oxidation state (rock salt, monoclinic, metal). Moreover, the copper proportions in the spherical structures on top of the nanorods formed with φ-1.05 accounted for 26.24% of all elements, including oxygen, whereas the elemental proportions of copper in the nanorod structures were only approximately 5.63% (Supplementary Fig. S5c, d). Dual confirmation with the EDS compositions and the copper XRD peaks for the φ-1.05 mixture indicated that the metallic Cu formed clusters that provided higher Cu proportions at the tops of the nanorods. Among the metal elements used for the HEO syntheses, copper was preferentially segregated and formed clusters, and this trend was explained by the Jahn-Teller behavior and size-related effects[24]. The segregated copper metal served as a catalyst reducing the oxygen atmosphere to O^{2-} with gaseous CuO, which generated the high-entropy rock-salt nanorods[25]. The configurational entropy was determined to be approximately 1.6R. This analysis confirmed that the combustion synthesis resulted in a tunable high-configurational entropy oxide based on optimization of the fuel-to-oxidizer ratio, although copper separation occurred for the high φ cases (1.0 and 1.05). EDS maps of the porous backbones that were not covered with spherical particles clearly elucidated the elemental distributions in the local areas (Supplementary Fig. S6). Slightly higher copper atomic ratios were observed for the composites fabricated with φ-0.9, and the other composites presented lower proportions of copper owing to segregation and transfer of the copper from the bulk metal oxide to the spherical surface particles. The configurational entropy was greater than 1.567R, indicating that all composites fabricated with the combustion synthesis were sufficiently mixed. Only the spherical particles in the composite with φ-1.05 had a low entropy of 1.428R, which was induced by the extruded copper metal species.

Specific characteristics of the fabricated HEOs were investigated with transmission electron microscopy (TEM), EDS, and selected area electron diffraction (SAED) analyses. In the TEM images of all samples, small grains and many grain boundaries appeared for the φ-0.9 composite (Fig. 4a), yet the grains gradually grew in all composites, including those synthesized with φ-0.95, φ-1.0 and φ-1.05 (Fig. 4b–d). A more intriguing feature was that a thin amorphous carbon layer covered the entire surfaces of the nanoparticles. Oxygen deficiencies at the interfaces between the particles and the ambient atmosphere led to incomplete combustion, thereby retaining some carbon species[26]. The presence of the spinel and rock-salt phases was confirmed by measuring the lattice fringe spacing and selected area electron diffraction (SAED) patterns. First, lattice fringe spacings of 0.253 nm and 0.242 nm, which corresponded to the (311) planes of the spinel phase and the (111) planes of the rock-salt phase, were observed for all HEO composites (Fig. 4e–h). Furthermore, the detected diffraction rings in the SAED patterns showed spinel phases for all cases (Fig. 4i–l). In particular, the diffraction patterns of the HEOs fabricated with φ-0.9 presented broad rings with some dots, indicating that this phase comprised the amorphous spinel with some polycrystalline areas (Fig. 4i). However, the rock salt diffraction dots, which are classified as spinel diffraction dots, gradually appeared in the HEO composites with φ-0.95, φ-1.0, and φ-1.05 (Fig. 4j–l). As the fuel-to-oxidizer ratio (φ) was increased, the combustion reactions became more active, which increased the

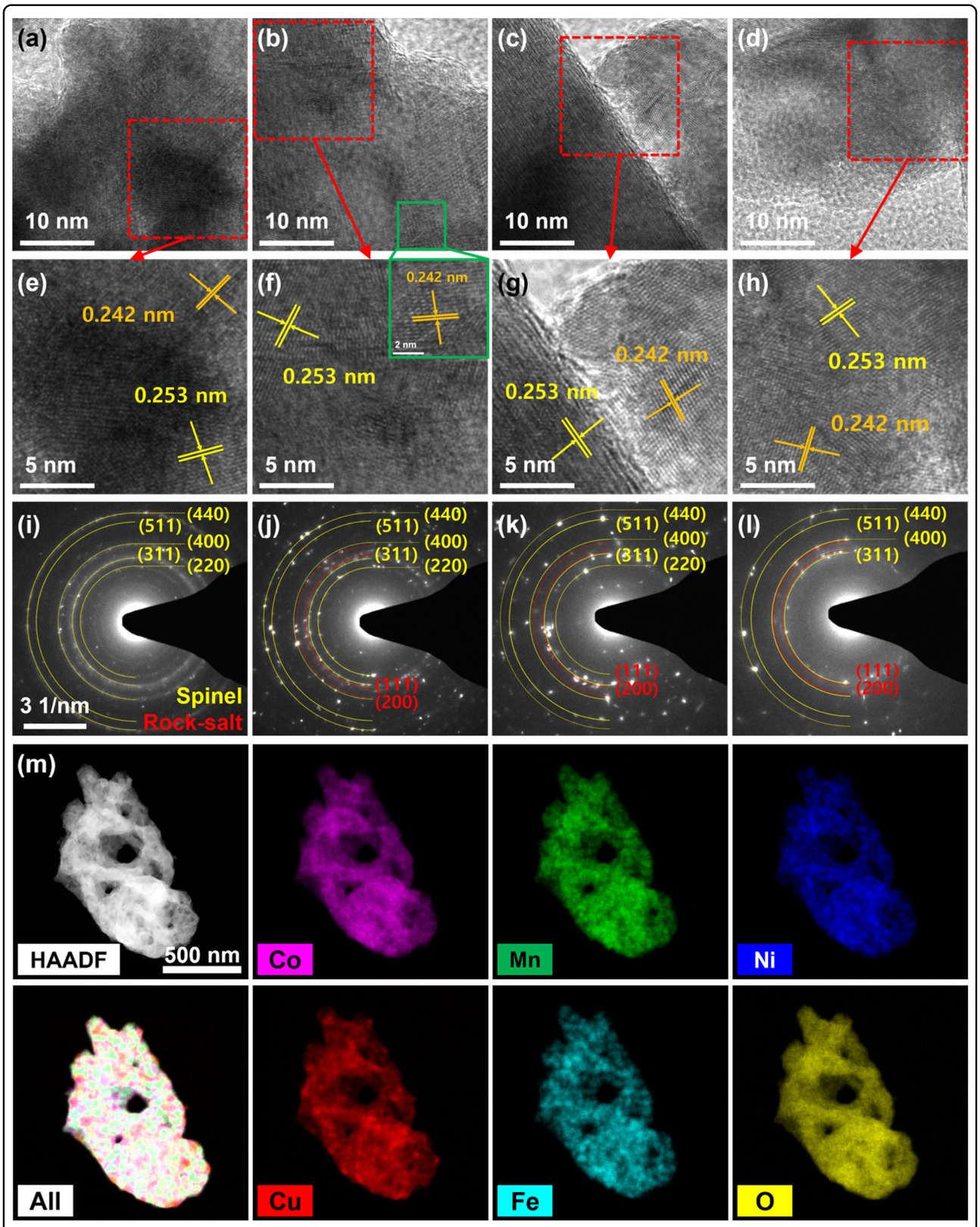

Fig. 4 (See legend on next page.)

(see figure on previous page)

Fig. 4 Phase transitions of the HEO composites enabled by the tunable combustion synthesis. High-resolution transmission electron microscopy (TEM) images of HEO composites fabricated with different fuel-to-oxidizer ratios of (**a**) φ-0.9, (**b**) φ-0.95, (**c**) φ-1.0, and (**d**) φ-1.05. Magnified inset images of the TEM images show the fringes of the HEO composites fabricated with (**e**) φ-0.9, (**f**) φ-0.95, (**g**) φ-1.0, and (**h**) φ-1.05. SAED patterns of HEO composites indicating spinel and rock-salt mixed phases fabricated with different fuel-to-oxidizer ratios of (**i**) φ-0.9, (**j**) φ-0.95, (**k**) φ-1.0, and (**l**) φ-1.05. (**m**) EDS mapping images of the HEO composite fabricated with φ-0.95. Homogeneously distributed metal and oxygen elements are observed, while a partial separation of Cu occurred.

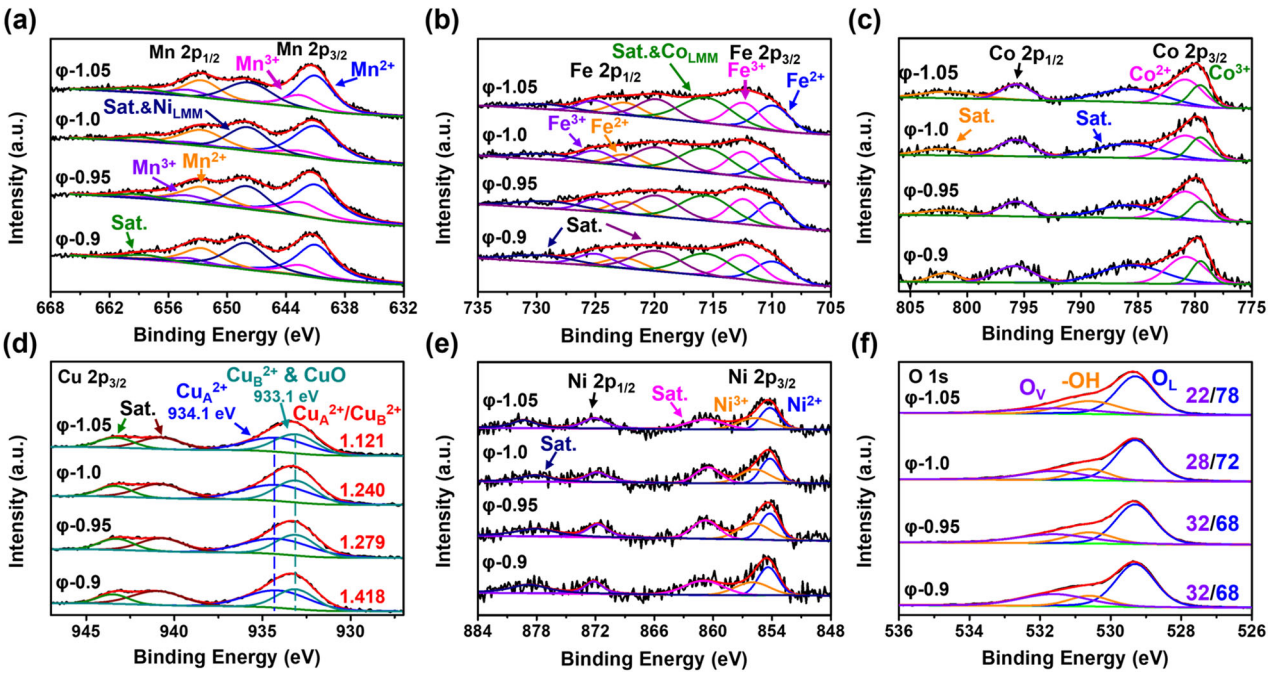

Fig. 5 Valence and component transitions of the HEO composites prepared with tunable combustion syntheses. (**a**) Mn 2p, (**b**) Fe 2p, (**c**) Co 2p, (**d**) Cu 2p, (**e**) Ni 2p, and (**f**) O 1s XPS data for HEO composites fabricated with different fuel-to-oxidizer ratios (φ-0.9, φ-0.95, φ-1.0, and φ-1.05).

reaction temperature and consumed more oxygen. This synthetic environment resulted in the production of a highly crystalline metal oxide and a low oxygen composition. The compositional homogeneity resulting from the synthetic conditions was confirmed with the EDS maps (Fig. 4m, Supplementary Fig. S7).

All of the fuel-to-oxidizer ratios used in the syntheses of the HEO composites resulted in five homogeneously distributed metal elements, although partial separation of the Cu was observed for the φ-0.9, φ-1.0 and φ-1.05 mixtures (Supplementary Fig. S7). In the φ-0.9 case, thermal reduction and reoxidation of copper, subjected to the surrounding carbon shells, might have produced the monoclinic CuO peaks seen in the XRD dataset (Fig. 2). Meanwhile, the homogeneous distributions of multiple atoms in the inner particles indicated that low φ values led to the coexistence of amorphous and low-crystalline spinel and rock-salt HEO phases involving thin CuO shells formed via modulated combustion. As the fuel-to-oxidizer ratio was changed to φ-0.95, the elevated combustion temperature increased the thermal entropy ($T\triangle S_{thermal}$) and generated a negative Gibbs free energy for the transition, thereby resulting in crystallization of the stable HEO phases (Fig. 4m). When the higher φ values (φ-1.0 and φ-1.05) generated reducing environments in the syntheses, more separated Cu appeared in the EDS mapping data (Supplementary Fig. S7). This trend was consistent with the results of the XRD and SEM/EDS analyses. In particular, the Cu fraction that generated the rock-salt nanorods (Fig. 3l) was completely reduced to the metal for φ-1.05.

X-ray photoelectron spectroscopy (XPS) was used to investigate the valences and components of the HEO composites made with different fuel-to-oxidizer ratios for the combustion syntheses (Fig. 5). The core Mn 2p, Fe 2p, Co 2p, Cu 2p, Ni 2p, and O 1s XPS data obtained for the different φ values (0.9, 0.95, 1.0, 1.05) clarified the specific characteristics of the constituent elements in the HEO

composites, with precisely tuned phases corresponding to the synthetic conditions. The Mn 2p spectra were deconvoluted to give Mn^{2+} (641.0 and 652.6 eV) and Mn^{3+} (642.5 and 654.0 eV) peaks (Fig. 5a)[27]. Fading of the Mn^{3+} peak area in the XPS data showed that Mn favored the formation of a rock-salt phase at higher φ. The Ni_{LMM} auger spectra overlapped with the satellite peaks for Mn[28]. Meanwhile, the Fe 2p spectra were deconvoluted into Fe^{2+} peaks at 709.9 and 722.5 eV and Fe^{3+} peaks at 712.4 and 725.0 eV (Fig. 5b)[29–31]. The Co_{LMM} auger peak at 716.6 eV overlapped with the satellite peaks for Fe^{2+} and Fe^{3+}. The Co 2p spectra were deconvoluted into a Co^{2+} peak at 779.5 and a Co^{3+} peak at 780.8 (Fig. 5c)[32]. Because the specific areas of the Co^{3+} and Fe^{3+} peaks decreased as the fuel-to-oxidizer ratio was increased, reduction from the spinel to the rock-salt phase was confirmed by these analyses. Meanwhile, the Cu XPS data revealed distinct features indicating copper oxide separation (Fig. 5d). The two main Cu $2p_{3/2}$ peaks were located at approximately 933.1 eV and 934.1 eV for all HEO composites. The first was assigned to CuO and Cu^{2+} in the octahedral sites ($Cu_B{}^{2+}$) of the spinel phase and the second to Cu^{2+} in the tetrahedral sites ($Cu_A{}^{2+}$) of the spinel phase[33,34]. The significant feature was that the ratio of the peak areas ($Cu_A{}^{2+}/Cu_B{}^{2+}$) decreased with increases in the fuel-to-oxidizer ratios because the strong reducing atmosphere led to CuO formation. In the Ni 2p XPS data, the $2p_{3/2}$ peaks centered at 854.4 eV and 856 eV were assigned to Ni^{2+} and Ni^{3+}, respectively (Fig. 5e)[14]. The Ni^{3+} peak showed a decreased peak area due to reduction as the fuel-to-oxidizer ratio was increased. Last, there were three O 1 s peaks located at 529.3 eV, 530.6 eV, and 531.6 eV, which represented lattice oxygens, chemisorbed oxygen and oxygen vacancies, respectively (Fig. 5f)[27]. Based on a precise investigation of the dataset, the proportions of oxygen vacancies were lower in the larger particles produced with higher φ values; the O_V/O_L ratios for the φ-1.05 and φ-0.9 mixtures were 22/78 and 32/68, respectively. They were typically formed on the surfaces of the smaller nanoparticles, which were produced with the lower φ values.

The precisely tuned HEO composites manufactured with different fuel-to-oxidizer ratios (φ) offered a rational design strategy resulting in the desired structures and phase compositions for the five cation precursors (Fig. 6). The lean fuel mixtures (φ-0.9 and φ-0.95) resulted in relatively porous structures with small particles and grain sizes, and the resulting HEO exhibited mixed spinel and rock-salt phases. With a lean fuel mixture (φ-0.9), a small amount of copper was reduced by the carbon residue from incomplete combustion, and the reduced Cu was reoxidized, resulting in CuO segregation on the surface. Additionally, with moderately lean fuel mixtures (φ-0.95), the elevated combustion temperature provided enough thermal entropy ($T\Delta S_{thermal}$) to achieve entropic stabilization and a mean optimized φ for the HEO synthesis. Furthermore, the higher fuel-to-oxidizer ratios (φ-1 and φ-1.05) resulted in agglomeration, thereby leading to lower porosities and larger particles. Additionally, because the excessively reducing atmosphere (φ-1.05) produced

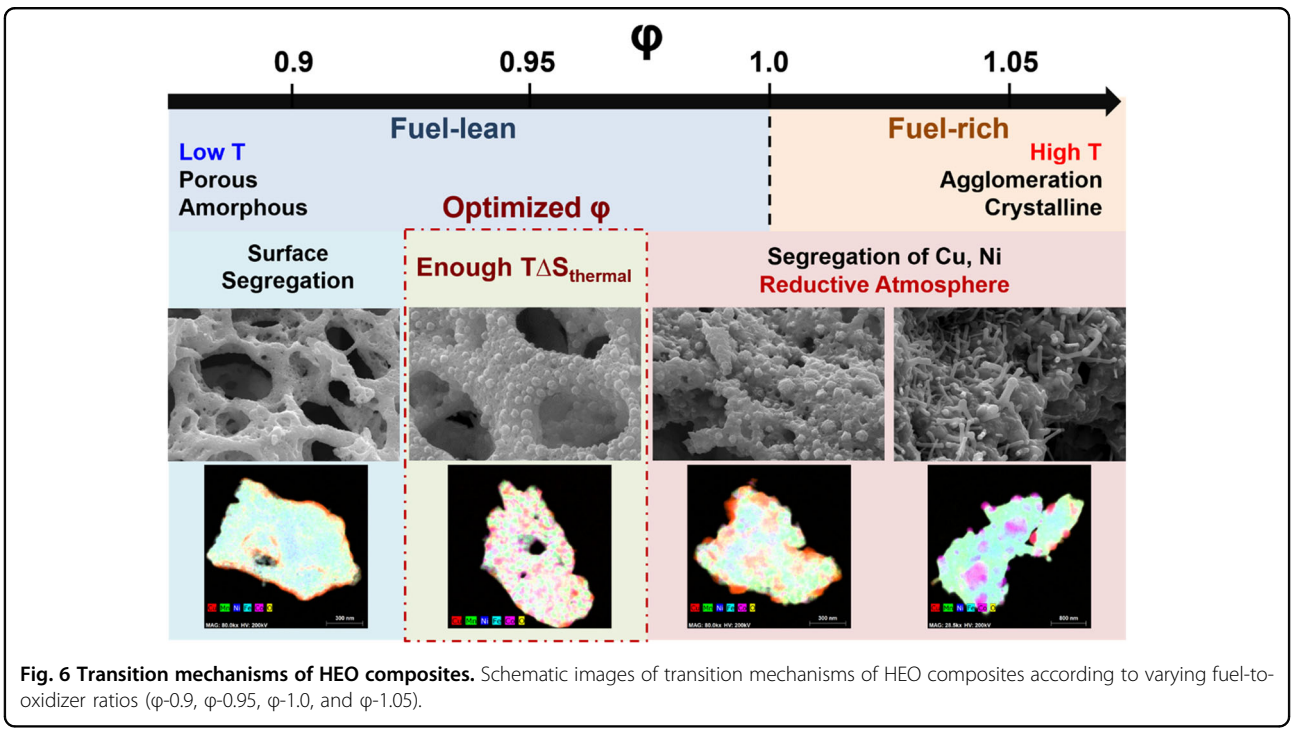

Fig. 6 Transition mechanisms of HEO composites. Schematic images of transition mechanisms of HEO composites according to varying fuel-to-oxidizer ratios (φ-0.9, φ-0.95, φ-1.0, and φ-1.05).

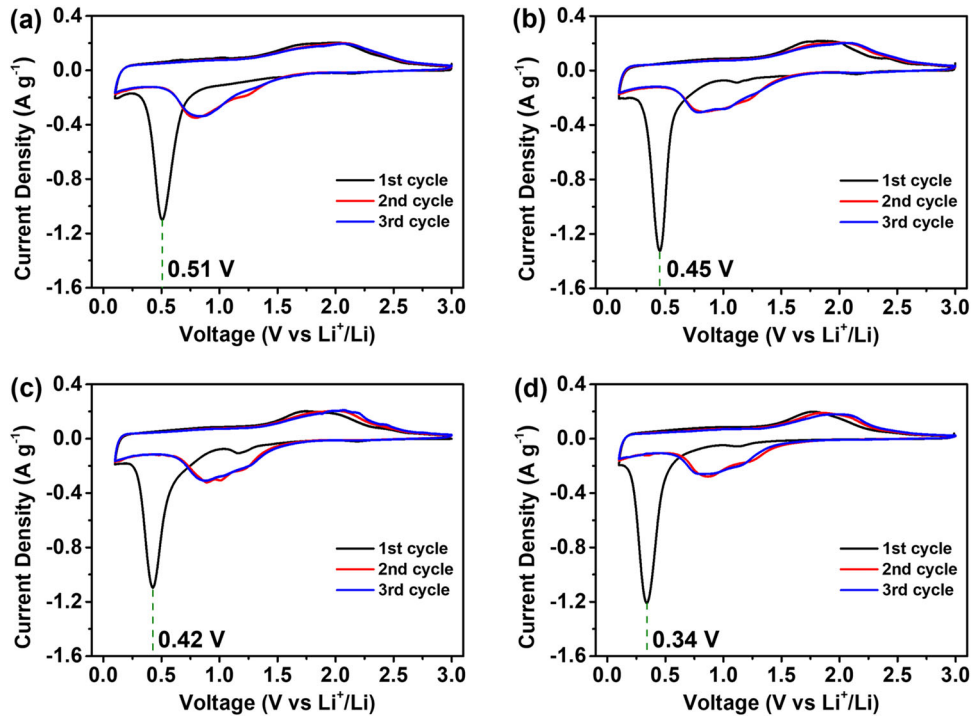

Fig. 7 Electrochemical characteristics of HEO-based LIB electrodes during initial cycles. Cyclic voltammetry curves for electrodes fabricated from HEO composites with different fuel-to-oxidizer ratios of (**a**) φ-0.9, (**b**) φ-0.95, (**c**) φ-1.0, and (**d**) φ-1.05 at a scan rate of 0.1 mV s^{-1} in the voltage range 0.01–3.00 V.

more Cu separation and even dispersed the Ni during combustion, the highest proportion of the monoclinic CuO phase, 7.53%, was observed for the stoichiometric fuel-to-oxidizer ratio (φ-1), as calculated with the Rietveld refinement (Supplementary Table S1). The separation of copper led to the formation of a secondary rock-salt phase that contained more copper and nickel than other cations. Finally, because the metallic Cu produced with the high fuel-to-oxidizer ratio of φ-1.05 served as an oxygen-reducing catalyst promoting nanorod growth, the rock-salt nanorods with Cu-metal nanoparticles were formed.

Electrochemical capabilities of the tunable HEO-based LIB anodes

The HEO composites synthesized with the different fuel-to-oxidizer ratios were used as the active materials in the HEO anodes with carbon black and the CMC/SBR binder. Afterward, the fabricated HEO anodes were evaluated in half-cells with Li-metal counter electrodes. The cyclic voltammograms (CV) generated with scan rates of 0.1 mVs^{-1} over the potential range 0.01 to 3 V showed the electrochemical features resulting from changes in the structures and phases of the HEO anodes (Fig. 7). Distinct cathodic peaks between 0.34 and 0.51 V in the first charge–discharge cycle indicate conversions of the metal oxides into metallic Mn, Fe, Co, Ni, Cu and a Li_2O matrix, as well as the formation of an SEI layer (Fig. 7a–d)[12,35]. The shifts of the cathodic peaks from 0.51 V to 0.34 V resulted from reductions of the metal oxides after transition from the spinel phase to the rock-salt phase and reduction of the monoclinic metal oxides to the cubic metal phases with the higher fuel-to-oxidizer ratios. Irreversible CV curves were observed in the first charge–discharge cycle, which is typical of HEO anodes and results from the initial lithiation process[13,36]. Meanwhile, the broad anodic peak seen between 1.7 and 2 V in the first anodic scan indicated oxidation of the metallic Mn, Fe, Co, Ni, and Cu[37]. After the first charge–discharge cycle, all of the CV curves for the HEO anodes synthesized with various fuel-to-oxidizer ratios showed outstanding electrochemical reversibility, as demonstrated by the overlapping curves.

The electrochemical capabilities of the HEO anodes were determined from the reaction rates. Electrochemical impedance spectroscopy was applied after the rate test, followed by the determination of long-term charge–discharge retention (Fig. 8). First, the charge–discharge voltage profiles determined at 0.2 A g^{-1} for φ-0.9, φ-0.95, φ-1.0, and φ-1.05 in the first cycle exhibited voltage plateaus near 0.7 V in the discharge curves, which indicated the formation of an SEI film and a conversion reaction (Fig. 8a). This was consistent with the typical phenomena

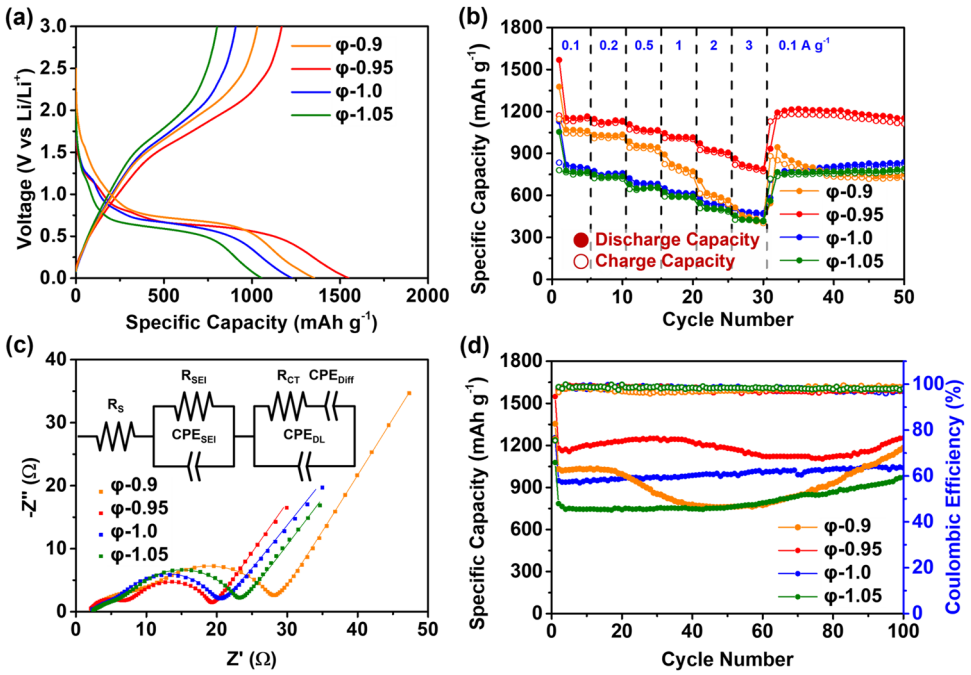

Fig. 8 Electrochemical properties of HEO-based LIB electrodes fabricated via tunable combustion syntheses. a Discharge–charge voltage profiles for the first cycle, (**b**) rate capability tests performed at several current densities (0.1, 0.2, 0.5, 1, 2, 3, 0.1 A g^{-1}), **c** EIS analyses performed after the rate capability tests, and (**d**) long-term charge–discharge stabilities at a current density of 0.2 A g^{-1} over 100 cycles for electrodes employing HEO composites fabricated with different fuel-to-oxidizer ratios (φ-0.9, φ-0.95, φ-1.0, and φ-1.05).

observed with CV curves (Fig. 7). In the voltage drop region, the completely reduced metal particles were involved in the lithium storage process, which resulted in additional capacity beyond the theoretical limit for the transition metal-oxide anodes[38]. The initial discharge capacities were 1354, 1549, 1227, and 1055 mAh g^{-1} for the φ-0.9, φ-0.95, φ-1.0, and φ-1.05 samples, respectively, and the initial Coulombic efficiencies (ICEs) were 76.1, 75.4, 73.9, and 76.0%, respectively. The conversion-type metal-oxide anode materials were lithiated according to the following electrochemical redox processes:

$$M_3O_4 + 8Li^+ + 8e^- \rightarrow 4Li_2O + 3M \quad (2)$$

Spinel phases

$$MO + 2Li^+ + 2e^- \rightarrow Li_2O + M \quad (3)$$

Rock salt, monoclinic CuO phase (M = Fe, Mn, Co, Ni, Cu; transition metals)

Metal oxides with higher oxidation states store more lithium ions in the Li_2O phase through multiple redox reactions. Consequently, the HEO anode synthesized with φ-0.95, which had the highest proportion of the spinel phase, exhibited the highest capacity because of its higher oxidation states and higher metal-oxide entropy. Formation of the SEI and electrolyte degradation were primarily responsible for the irreversible capacity loss of the first charge–discharge cycle. SEI formation was inhibited when a higher fuel-to-oxidizer ratio was used in the synthetic process to give larger HEO particles. In contrast, the Cu oxide nanorods grown in the HEO anodes (φ-1.05) enhanced SEI formation because of the extended active surface area resulting from the one-dimensional nanostructures.

The capacities and rates of the HEO anodes were investigated as a function of the fuel-to-oxidizer ratios with different current densities ranging from 0.1 to 3 A g^{-1} (Fig. 8b). The HEO anodes based on the φ-0.9, φ-0.95, φ-1.0, and φ-1.05 mixtures showed reversible capacities of 1062, 1165, 795 and 770 mAh g^{-1} for the first 5 cycles, respectively, at a rate of 0.1 A g^{-1}.

The rate capabilities were calculated from the discharge capacity measured with a current density of 3 A g^{-1} after the 30th cycle and compared with the discharge capacity seen for a current density of 0.1 A g^{-1} after the 5^{th} cycle. These were 39.5%, 67.8%, 59.1%, and 54.5%, for the φ-0.9, φ-0.95, φ-1.0, and φ-1.05 samples, respectively, and the lowest rate was seen for the φ-0.9 ratio. The charge transfer resistance of the grain boundaries could have increased at φ-0.9 because the grains were too small and porous, which was supported by the EIS results (Fig. 8c). Additionally, as shown by the EIS results, the φ-1.0 and φ-1.05 samples exhibited lower rates than the φ-0.95 sample because more aggregates were formed at the high

temperatures of the combustion processes, resulting in slight increases in the charge transfer resistances. Although the spinel and rock-salt phases appeared in the HEO composites fabricated with φ-0.9, capacity degradation was observed. This occurred because the highly porous structures with small particle dimensions and weak connections between the constituents did not withstand the structural damage caused by the uneven forces exerted during rapid conversion of the lithium ions and primary nanoparticles, which had large surface activities (Fig. 3a). In contrast, the HEO composites prepared with the optimal fuel-to-oxidizer ratio (φ-0.95) exhibited the highest specific capacities and rates owing to the continuously connected backbone networks and moderately porous structures that inhibited structural damage and volume expansion. Furthermore, the homogeneously mixed HEO phases exhibited an entropy stabilization effect. Meanwhile, when the fuel-to-oxidizer ratios were φ-1.0 and φ-1.05, connected backbones and outstanding rate capabilities were obtained (Fig. 3c, d and Fig. 8b). However, the HEO anodes fabricated with the stoichiometric and excess fuel-to-oxidizer ratios revealed lower capacities than those fabricated with the optimal fuel-to-oxidizer ratio (φ-0.95) because of the highly reduced and separated copper-nickel species with low oxidation states and configurational entropies. When the HEO anodes were subjected to 50 cycles, including an additional 20 cycles, at a rate of 0.1 A g^{-1}, the capacities for the φ-0.9, φ-0.95, φ-1.0, and φ-1.05 ratios were 754, 1151, 839 and 790 mAh g^{-1}, respectively. The best performance was still that of the φ-0.95 anode, although it underwent a rapid decay in capacity from 1062 mAh g^{-1} (5th cycle).

Electrochemical impedance spectroscopy (EIS) was used after 50 cycles to determine the rate capabilities in the discharged state and elucidate the electrochemical features of the HEO anodes (Fig. 8c). An equivalent circuit comprising R_S, R_{SEI}, R_{CT}, CPE_{SEI}, CPE_{Diff}, and CPE_{DL} was applied to the EIS data to represent the solution resistance, SEI resistance, charge transfer resistance, and constant phase elements for the SEI, lithium-ion diffusion, and electrical double-layer capacitance, respectively (Supplementary Fig. S8). Based on the fitted components of the equivalent circuit, the R_{SEI} clarified the capacities seen for the different fuel-to-oxidizer ratios. The highest R_{SEI} value was seen for the φ-0.9-based HEO anode, which indicated that the excess SEI caused a rapid loss of capacity during the rate capability measurement. Considerable SEI formation was attributed to the large surface areas of the porous structures formed with the smallest nanoparticles, which enabled continuous infiltration of the electrolyte into the pores. In contrast, the extracted R_{SEI} values decreased as the fuel-to-oxidizer ratio (φ) was increased because the proper dimensions of the nanoparticles and a moderate level of structural agglomeration suppressed SEI formation. Additionally, the HEO anodes with the φ-0.95 and φ-1.0 ratios presented low R_{CT} values of 11.5 and 9.8 Ω, respectively, which contributed to their high rates. The excess SEI served as a barrier inhibiting Li^+ transfer between the electrolyte and the anode, and aggregation of the active material inhibited charge transport with a small interfacial area, as shown by the large R_{CT} values for the φ-0.9 and φ-1.05 ratios.

The long-term cycling performance of the HEO anodes over 100 cycles with a rate of 0.2 A g^{-1} indicated a correlation between the synthetic conditions (φ-0.9, 0.95, 1.0, and 1.05) and the electrochemical stabilities of the resulting anodes (Fig. 8d). All of the HEO composites manufactured with the different fuel-to-oxidizer ratios exhibited outstanding cycling stability over 100 cycles. In particular, for the HEO with the φ-0.95 ratio, the highest discharge capacity of 1252 mAh g^{-1} was obtained for 100 cycles, compared with discharge capacities of 1040, 1184, and 972 mAh g^{-1} for the φ-0.9, φ-1.0, and φ-1.05 ratios, respectively; this resulted from the high oxidation state, superior structural stability and low R_{CT} value of the φ-0.95 system. The increasing trends seen for the capacity curves in some cycles were attributed to activation induced by electrolyte infiltration into the pores. Meanwhile, the rapid decay of the specific capacity seen during the initial 50 cycles for the HEO anode made with the φ-0.9 ratio was attributed to the low structural stability and excess SEI formation resulting from the highly porous and weakly connected backbone, as well as permanent conversion of the CuO into metallic Cu on the surfaces of the HEO particles[10]. Although the φ-0.9-based electrode exhibited severe capacity fading in the early stages, the rationally designed HEO electrodes with the optimal fuel-to-oxidizer ratios exhibit remarkable cycling stabilities over 100 cycles, which significantly exceeded those of conventional conversion-type anodes[39]. These outcomes confirmed that the entropy stabilization effect of the developed HEO materials facilitated stable conversion reactions. Finally, the Coulombic efficiencies of all HEO electrodes were maintained above approximately 98% over 100 cycles, thereby indicating very little loss in the Coulombic efficiencies due to activation processes.

Compared to the electrochemical capabilities of other HEO-based electrodes, the $(FeCoNiCrMn)_3O_4$ material with a spinel structure, which was prepared by D. Wang et al., delivered a specific capacity of 586 mAh g^{-1} at 0.1 A g^{-1}. HEOs with identical elements were prepared by Xiao et al. and Nguyen et al. and delivered specific capacities of 625 mAh g^{-1} and 649 mAh g^{-1} at 1 A g^{-1}, respectively. The HEO electrodes developed with the optimized φ-0.95 ratio exhibited substantially higher specific capacities of 1165 mAh g^{-1} at 0.1 A g^{-1} and 1015 mAh g^{-1} at 1 A g^{-1} in the rate capability tests[14,15]. In

terms of scalability, the previous methods used to prepare HEO electrodes inevitably involved multistep and time-consuming synthetic processes. For instance, although the high-entropy spinel oxide synthesized by Huang et al. showed a good reversible capacity of 1170 mAh g^{-1} at 0.1 A g^{-1}, long-term processes and postheat treatment at a high temperature (~900 °C) were required to fabricate the HEO active materials[40]. In this respect, the facile development of HEO-based electrodes via combustion syntheses with controllable fuel-to-oxidizer ratios offers precisely tunable methods to secure both superior electrochemical performance and scalable fabrication strategies.

Conclusion

We developed a rational strategy for fabricating tunable HEO materials for highly stable conversion-type LIB anodes via a one-step combustion synthesis. Four different HEO products with specific phases and configurational entropies were synthesized with precisely controllable combustion processes and adjusted fuel-to-oxidizer ratios (φ-0.9, 0.95, 1.0, and 1.05). The crystalline structures exhibited the spinel and rock-salt phases, which provided entropy stabilization during the conversion reactions, and the transitions between phases and the porosities were tuned with the fuel-to-oxidizer ratios. Among the fabricated HEO composites, the φ-0.95-based LIB anode exhibited the best electrochemical performance due to the optimized porosity, particle dimensions, and crystallinity of the HEO active materials and the highly oxidized and electrochemically inactive metal-free phases. The resulting anode exhibited the highest initial discharge/charge specific capacity of 1549 mAh g^{-1} and an excellent rate capability of 67.8% at current densities of 0.1–3 A g^{-1}. Furthermore, superior cycling stability was observed at 1252 mAh g^{-1} after 100 cycles at 0.2 A g^{-1}. Precisely tunable HEOs synthesized by combustion syntheses enabled efficient screening of the optimal phases, structures, and configurational entropies of high-performance LIB electrodes. Furthermore, this facile yet scalable fabrication strategy for HEO materials will provide fascinating hybrid electrodes and catalysts that cannot be prepared with conventional fabrication methods.

Acknowledgements

This work was supported by the National Research Foundation of Korea (NRF) grant funded by the Korean government (Ministry of Science and ICT) (No. 2023R1A2C2006407, No. 2020R1A5A1018153).

Author contributions

D.J.S. and W.J.C. developed the overall concept and designed the technical approaches for HEO LIB anodes. D.J.S. and S.H.C. fabricated the HEO composites using combustion syntheses with different fuel-to-oxidizer ratios and investigated their electrochemical properties as LIB anodes. D.J.S., S.H.C., S.H.P., and B.S.S. analyzed the phases, morphologies and chemical compositions using various equipment. D.J.S., S.H.C., and W.J.C. interpreted the data and wrote the manuscript.

Conflict of interest

The authors declare no competing interests.

Publisher's note

Springer Nature remains neutral with regard to jurisdictional claims in published maps and institutional affiliations.

Supplementary information The online version contains supplementary material available at https://doi.org/10.1038/s41427-023-00502-y.

Received: 9 June 2023 Revised: 18 August 2023 Accepted: 22 August 2023.
Published online: 13 October 2023

References

1. Zeng, X. et al. Commercialization of lithium battery technologies for electric vehicles. *Adv. Energy Mater.* **9**, 1900161 (2019).
2. Zhang, X., Xu, X., Hu, Y., Xu, G., He, W. & Zhu, J. $C_{60}/Na_4FeO_3/Li_3V_2(PO_4)_3$/soft carbon quaternary hybrid superstructure for high-performance battery-supercapacitor hybrid devices. *NPG Asia Mater.* **12**, 8 (2020).
3. Wu, Y., Rahm, E. & Holze, R. Carbon anode materials for lithium ion batteries. *J. Power Sources* **114**, 228–236 (2003).
4. Pang, H. et al. Super-assembled compressible carbon frameworks featuring enriched heteroatom defect sites for flexible Znâ€"air batteries. *NPG Asia Mater.* **15**, 15 (2023).
5. Fang, S., Bresser, D. & Passerini, S. Transition metal oxide anodes for electrochemical energy storage in lithium-and sodium-ion batteries. *Adv. Energy Mater.* **10**, 1902485 (2020).
6. Lee, S.-H., Kim, K.-Y. & Yoon, J.-R. Binder-and conductive additive-free laser-induced graphene/$LiNi_{1/3}Mn_{1/3}Co_{1/3}O_2$ for advanced hybrid supercapacitors. *NPG Asia Mater.* **12**, 28 (2020).
7. Jiang, Y. et al. Highly porous Mn_3O_4 micro/nanocuboids with in situ coated carbon as advanced anode material for lithium-ion batteries. *Small* **14**, 1704296 (2018).
8. Lee, S. H. et al. Self-assembled Fe_3O_4 nanoparticle clusters as high-performance anodes for lithium ion batteries via geometric confinement. *Nano Lett.* **13**, 4249–4256 (2013).
9. Sarkar, A. et al. High-entropy oxides: fundamental aspects and electrochemical properties. *Adv. Mater.* **31**, 1806236 (2019).
10. Marques, O. J., Chen, C., Timofeeva, E. V. & Segre, C. U. Local structure and conversion chemistry of high-entropy oxides as Li-ion anodes. *J. Power Sources* **564**, 232852 (2023).
11. Marques, O. J., Walter, M. D., Timofeeva, E. V. & Segre, C. U. Effect of initial structure on performance of high-entropy oxide anodes for li-ion batteries. *Batteries* **9**, 115 (2023).
12. Choi, C. et al. Achieving high energy density and high power density with pseudocapacitive materials. *Nat. Rev. Mater.* **5**, 1–15 (2019).
13. Lokcu, E., Toparli, C. & Anik, M. Electrochemical performance of $(MgCoNiZn)_{1-x}Li_xO$ high-entropy oxides in lithium-ion batteries. *ACS Appl. Mater. interfaces* **12**, 23860–23866 (2020).
14. Nguyen, T. X., Patra, J., Chang, J.-K. & Ting, J.-M. High entropy spinel oxide nanoparticles for superior lithiation–delithiation performance. *J. Mater. Chem. A* **8**, 18963–18973 (2020).
15. Wang, D. et al. Spinel-structured high entropy oxide $(FeCoNiCrMn)_3O_4$ as anode towards superior lithium storage performance. *J. Alloy. Compd.* **844**, 156158 (2020).
16. Nguyen, T. X., Tsai, C.-C., Patra, J., Clemens, O., Chang, J.-K. & Ting, J.-M. Co-free high entropy spinel oxide anode with controlled morphology and crystallinity for outstanding charge/discharge performance in Lithium-ion batteries. *Chem. Eng. J.* **430**, 132658 (2022).
17. Qiu, N., Chen, H., Yang, Z., Sun, S., Wang, Y. & Cui, Y. A high entropy oxide (Mg0. 2Co0. 2Ni0. 2Cu0. 2Zn0. 2O) with superior lithium storage performance. *J. Alloy. Compd.* **777**, 767–774 (2019).
18. Rost, C. M. et al. Entropy-stabilized oxides. *Nat. Commun.* **6**, 1–8 (2015).
19. Yu, P. et al. Preparation of high entropy $(Ba_{0.2}Mg_{0.2}Ca_{0.2}Sr_{0.2}Pb_{0.2})TiO_3$ perovskite oxide powders by a sol-hydrothermal method. *Ceram. Int.* **48**, 15992–15999 (2022).

20. Yao, Y. et al. Carbothermal shock synthesis of high-entropy-alloy nanoparticles. *Science* **359**, 1489–1494 (2018).
21. Aydinyan, S., Kirakosyan, H., Sargsyan, A., Volobujeva, O. & Kharatyan, S. Solution combustion synthesis of MnFeCoNiCu and $(MnFeCoNiCu)_3O_4$ high entropy materials and sintering thereof. *Ceram. Int.* **48**, 20294–20305 (2022).
22. Saghir, A. V., Beidokhti, S. M., Khaki, J. V. & Salimi, A. One-step synthesis of single-phase (Co, Mg, Ni, Cu, Zn) O High entropy oxide nanoparticles through SCS procedure: thermodynamics and experimental evaluation. *J. Eur. Ceram. Soc.* **41**, 563–579 (2021).
23. Aali, H., Mollazadeh, S. & Khaki, J. V. Single-phase magnetite with high saturation magnetization synthesized via modified solution combustion synthesis procedure. *Ceram. Int.* **44**, 20267–20274 (2018).
24. Anand, G., Wynn, A. P., Handley, C. M. & Freeman, C. L. Phase stability and distortion in high-entropy oxides. *Acta Materialia* **146**, 119–125 (2018).
25. Tai, K., Sun, K., Huang, B. & Dillon, S. J. Catalyzed oxidation for nanowire growth. *Nanotechnology* **25**, 145603 (2014).
26. Shin, D., Shin, J., Yeo, T., Hwang, H., Park, S. & Choi, W. Scalable synthesis of triple-core–shell nanostructures of TiO_2@ MnO_2@ C for high performance supercapacitors using structure-guided combustion waves. *Small* **14**, 1703755 (2018).
27. Zhang, J., Sun, Y., Li, X. & Xu, J. Fabrication of porous $NiMn_2O_4$ nanosheet arrays on nickel foam as an advanced sensor material for non-enzymatic glucose detection. *Sci. Rep.* **9**, 1–13 (2019).
28. Azmi, R., Trouillet, V., Strafela, M., Ulrich, S., Ehrenberg, H. & Bruns, M. Surface analytical approaches to reliably characterize lithium ion battery electrodes. *Surf. Interface Anal.* **50**, 43–51 (2018).
29. Gong, Y. et al. Inverse spinel cobalt–iron oxide and n-doped graphene composite as an efficient and durable bifuctional catalyst for Li–O_2 batteries. *ACS Catal.* **8**, 4082–4090 (2018).
30. Wang, D. et al. Low-temperature synthesis of small-sized high-entropy oxides for water oxidation. *J. Mater. Chem. A* **7**, 24211–24216 (2019).
31. Xiang, H.-Z., Xie, H.-X., Chen, Y.-X., Zhang, H., Mao, A. & Zheng, C.-H. Porous spinel-type $(Al_{0.2}$ $CoCrFeMnNi)_{0.58}O_{4-\delta}$ high-entropy oxide as a novel high-performance anode material for lithium-ion batteries. *J. Mater. Sci.* **56**, 8127–8142 (2021).
32. Xu, L. et al. Plasma-engraved Co_3O_4 nanosheets with oxygen vacancies and high surface area for the oxygen evolution reaction. *Angew. Chem.* **128**, 5363–5367 (2016).
33. Zhao, H., Fang, K., Dong, F., Lin, M., Sun, Y. & Tang, Z. Textual properties of Cu–Mn mixed oxides and application for methyl formate synthesis from syngas. *J. Ind. Eng. Chem.* **54**, 117–125 (2017).
34. Faheem, M., Jiang, X., Wang, L. & Shen, J. Synthesis of Cu_2O–$CuFe_2O_4$ microparticles from Fenton sludge and its application in the Fenton process: the key role of Cu_2O in the catalytic degradation of phenol. *RSC Adv.* **8**, 5740–5748 (2018).
35. Ghigna, P. et al. Lithiation mechanism in high-entropy oxides as anode materials for Li-ion batteries: an operando XAS study. *ACS Appl. Mater. interfaces* **12**, 50344–50354 (2020).
36. Chen, H., Qiu, N., Wu, B., Yang, Z., Sun, S. & Wang, Y. A new spinel high-entropy oxide $(Mg_{0.2}Ti_{0.2}Zn_{0.2}$ $Cu_{0.2}Fe_{0.2})_3O_4$ with fast reaction kinetics and excellent stability as an anode material for lithium ion batteries. *RSC Adv.* **10**, 9736–9744 (2020).
37. Zhu, Y. P., Ma, T. Y., Jaroniec, M. & Qiao, S. Z. Self-templating synthesis of hollow Co3O4 microtube arrays for highly efficient water electrolysis. *Angew. Chem. Int. Ed.* **56**, 1324–1328 (2017).
38. Li, Q. et al. Extra storage capacity in transition metal oxide lithium-ion batteries revealed by in situ magnetometry. *Nat. Mater.* **20**, 76–83 (2021).
39. Li, J. et al. Phase evolution of conversion-type electrode for lithium ion batteries. *Nat. Commun.* **10**, 1–10 (2019).
40. Huang, C.-Y. et al. Atomic-scale investigation of lithiation/delithiation mechanism in High-entropy spinel oxide with superior electrochemical performance. *Chem. Eng. J.* **420**, 129838 (2021).